# *Optimizing nanoparticle perovskite for bifunctional oxygen electrocatalysis*

Energy & Environmental Science

RSCPublishing

PAPER

# Optimizing Nanoparticle Perovskite for Bifunctional Oxygen Electrocatalysis

Cite this: DOI: 10.1039/x0xx00000x

Jae-Il Jung[1], Marcel Risch[2], Seungkyu Park[1], Min Gyu Kim[3], Gyutae Nam[1], Hu-Young Jeong[4], Yang Shao-Horn*[2] and Jaephil Cho*[1]

Received ooth May 2015,
Accepted ooth May 2015

DOI: 10.1039/x0xx00000x

www.rsc.org/

Highly efficient bifunctional oxygen electrocatalysts are indispensable to the development of highly efficient regenerative fuel cells and rechargeable metal-air batteries, which could power future electric vehicles. Although perovskite oxides are known to have high intrinsic activity, large particle sizes rendered from traditional synthesis routes limit their practical use due to low mass activity. We report the synthesis of nano-sized perovskite particles with a nominal composition of $La_x(Ba_{0.5}Sr_{0.5})_{1-x}Co_{0.8}Fe_{0.2}O_{3-\delta}$ (BSCF), where lanthanum concentration and calcination temperature were controlled to influence oxide defect chemistry and particle growth. This approach produced a bifunctional perovskite electrocatalyst of ~50 nm size with supreme activity and stability for both the oxygen reduction reaction (ORR) and oxygen evolution reaction (OER). The electrocatalyst preferentially reduced oxygen to water (<5 % peroxide yield), exhibited more than 20 times higher gravimetric activity (A/g) than $IrO_2$ in an OER half-cell test (0.1 M KOH), and surpassed the charge/discharge performance of Pt/C (20 wt%) in a zinc-air full cell test (6 M KOH). Our work provides a general strategy for designing perovskite oxides as inexpensive, stable and highly active bifunctional electrocatalysts for future electrochemical energy storage and conversion devices.

**Broader context**

The world-wide interest in reducing the dependency on fossil fuels demands the development of energy storage systems with high power density from abundant materials, which would enable wide-spread industrial deployment of grid-scale renewable energy systems, as well as the progressive advancement of high-powered electric vehicles (EVs). Perovskite oxide ceramics attracted significant attention as a strong candidate for bi-functional electrocatalyst for metal-air batteries. There has been consistent investigation on the viability of bi-functional electrocatalysts, because energy storage systems cannot operate rechargeably without the proper bi-functional electrocatalyst. Among various electrocatalysts for both oxygen evolution and reduction, making nano-particles from these materials for practical applications is a great challenge. The newly introduced pervovskite electrocatalyst of ~50 nm size preferentially reduced oxygen to water (< 5 % peroxide yield), exhibited more than 20 times higher gravimetric activity (A/g) than $IrO_2$ in an OER half-cell test, and surpassed the charge/discharge performance of Pt/C (20 wt%) in a zinc-air full cell test. This study describes substantially the systematic engineering of perovskite ceramics into such a bifunctional nanosized electrocatalyst with high stability and activity, which was also explained in detail from the aspect of defect chemistry.

The world-wide interest in reducing the dependency on fossil fuels demands the development of energy storage systems with high power density from abundant materials, which would enable wide-spread industrial deployment of grid-scale renewable energy systems, as well as the progressive advancement of high-powered electric vehicles (EVs).[1-3] Even though Li ion batteries (LIBs) are traditionally considered the most promising candidates for EV applications with their high cycle capability and energy efficiency, their insufficient gravimetric storage capacity (100~200 W h $kg^{-1}$) limits long-term application in EVs. Alternatively, rechargeable zinc–air batteries are being spotlighted as strong candidates due to their extremely high gravimetric energy density (470 W h $kg^{-1}$), low cost and environmentally friendly operation.[1, 4] In addition, zinc–air batteries are compact and light-weight because they employ a lighter air cathode, which makes use of oxygen from the air upon discharge. However, the rechargeable zinc–air batteries are still in their early stages of development because there are still some critical issues to overcome. For example, the compact and rechargeable zinc–air batteries operating with two-electrodes have to overcome limited

[1] *School of Energy and Chemical Engineering, Ulsan National Institute of Science and Technology (UNIST), Ulsan, 689-798, South Korea.* [2]*Electrochemical Energy Laboratory, Massachusetts Institute of Technology, 77 Massachusetts Ave., Cambridge, MA, 02139, USA.* [3]*Beamline Research Division, Pohang Accelerator Laboratory, Pohang University Science and Technology, Pohang 790-784, South Korea.* [4]*UNIST Central Research Facilities (UCRF), Ulsan National Institute of Science & Technology (UNIST) Ulsan 689-798, Korea.* ***E-mail:** shaohorn@mit.edu; jpcho@unist.ac.kr*

† Electronic Supplementary Information (ESI) available: Table S1, and Figure S1–S6. See DOI: 10.1039/b000000x/

life, high cost and lack of bi-functional catalysts.[5] In order to fabricate available rechargeable zinc−air batteries, it is urgently demanded that metal oxide-based bi-functional catalysts are developed that can catalyze satisfactorily both the oxygen reduction reaction (ORR) upon discharge and the oxygen evolution reaction (OER) upon charge. Unfortunately, the OER and ORR mechanisms on oxides are not well understood, neither are potential modifications of the surface during catalytic turnover.[6] The bi-functionality of the metal oxide catalyst has been proposed to be controlled by the facility of adopting different valence states through redox couples at the overpotentials of ORR and OER.[7-10] Among various metal oxide-based bi-functional electrocatalysts, $La_xCa_{1-x}MO_3$ (M=Co, Ni, Mn) perovskite oxides have attracted consistent attention as potential bi-functional catalysts for metal-air batteries and fuel-cell systems.[11-16] Further improvement of activity was achieved by using composite electrodes, e.g. core-corona structural bifunctional catalyst (CCBC) that consists of $LiNiO_3$ as the core supported on nitrogen-doped carbon nanotube, which can catalyze OER and ORR, respectively, in zinc-air batteries.[17] Generally, composite electrode systems are known to support higher bifunctional activity and durability as compared with those containing only a single material.[17] Recently, Suntivich et al. introduced $Ba_{0.5}Sr_{0.5}Co_{0.8}Fe_{0.2}O_{3-\delta}$ (BSCF) as an excellent OER catalyst, that has Co cations with $t_{2g}^5e_g^{\sim1.2}$ electronic configuration and exhibits the highest OER activity among perovskite oxides, and whose performance is one order higher than $IrO_2$ in OER activity.[18, 19] They also explained that any transition-metal-oxide perovskite, which has an $e_g$-filling ($\sigma^*$-orbital occupation) slightly below 1 shows maximum ORR activity.[20-22]

BSCF has a complex defect chemistry and demonstrates diverse structural transitions according to heat treatments and/or dopant additions.[23-26] It is a great challenge to take advantage of the dynamic defect chemistry of BSCF perovskite catalysts through diverse directions and methods to design active and stable bifunctional electrocatalysts for industrial applications. The electrochemical performance of perovskite catalysts in metal-air batteries can be significantly enhanced not only by modifying surface chemistry and structure (yielding high intrinsic activity at fixed loading), but also by reducing the particle size to the nanoscale (yielding gravimetric mass activity at fixed composition) using the synergic effect of synthesis temperature and doping conditions.[27] A series of studies were reported that $La(Ca,Co)O_3$ perovskite particles were heat-treated and comminuted to obtain the increased concentration of active sites via increased surface area in bi-functional oxygen electrocatalysts.[14-16] As an example, Bursell et al. synthesized 70-nm sized $LaCaMnO_3$ perovskite by quenching the sample to R.T. after calcining at 700 °C in air.[14] Such an effort of improving catalytic activity by synthesizing nanoparticles was also observed in SOFC system.[28] For instance, Ortiz-Vitoriano et al. synthesized 150 nm sized clusters of $La_{0.8}Ca_{0.2}Fe_{0.8}Ni_{0.2}O_{3-\delta}$ oxide particles via freeze drying and liquid mixing method, which would be used for the cathode material in SOFC.[28] There have been rarely reported systematic studies on the nanoscale perovskite electrocatalyst particles that could be used in rechargeable metal-air batteries.

Particularly, BSCF perovskite, which is nowadays spotlighted as a strong candidate of bi-functional electrocatalyst both in ORR and OER, is worthwhile to be investigated deeply in pursuit of nanosized particles as a way of breakthrough in the area of rechargeable metal-air batteries.[18, 20, 27, 29] From this aspect, this report could be a pioneering progenitor in reporting the systematic engineering of BSCF perovskite oxides into such an outstanding bifunctional nanosized electrocatalyst with high stability and activity. In this work, we introduce a ~50 nm sized La-doped BSCF perovskite catalyst, which displays outstanding OER and ORR performances in half-cell tests, and surpasses Pt/C 20% as an air-electrode catalyst in Zn-air full cell performance.

## Experimental

### Catalyst preparation

$La_x(Ba_{0.5}Sr_{0.5})_{1-x}Co_{0.8}Fe_{0.2}O_{3-\delta}$ ($La_x$-5582)($x$ = 0.1, 0.3, 0.5 and 0.7) powders were prepared using polymerized complex methods described previously.[1] The starting materials consisted of barium nitrate ($Ba(NO_3)_2$, ≥99.0% purity, Alfar Aesar Co.), strontium nitrate ($Sr(NO_3)_2$, ≥99.0% purity, Aldrich Chemical Co.), lanthanum (III) nitrate hexahydrate ($La(NO_3)_3{\cdot}6H_2O$, ≥99.9% purity, Alfar Aesar Co.), cobalt(II) nitrate ($Co(NO_3)_2{\cdot}6H_2O$, ≥99.0% purity, Alfar Aesar Co.), and iron(III) nitrate ($Fe(NO_3)_3{\cdot}9H_2O$, ≥98.0% purity, Alfar Aesar Co.). A 0.04 mol quantity of ethylenediamine tetraacetic acid (EDTA) was mixed with 40 ml of a 1M $NH_4OH$ solution to make a $NH_4$-EDTA buffer solution. Molar amounts of lanthanum (III) nitrate hexahydrate (x = 0.002, 0.006, 0.010 and 0.014 mol), barium nitrate (1-x = 0.009, 0.007, 0.005 and 0.003 mol) and strontium nitrate (1-x = 0.009, 0.007, 0.005 and 0.003 mol) as well as 0.016 mol of $Co(NO_3)_2{\cdot}6H_2O$ and 0.004 mol of $Fe(NO_3)_3{\cdot}9H_2O$ were added to the buffer solution to make the required stoichiometries of $La_x(Ba_{0.5}Sr_{0.5})_{1-x}Co_{0.8}Fe_{0.2}O_{3-\delta}$ ($La_x$-5582), respectively. Anhydrous citric acid (0.06 mol) was added, and the pH value was adjusted to 8 using 1N $NH_4OH$ solution. Each solution was kept on a hot plate at 100°C and stirred until gelation occurred. After 24 h, the gelled samples were baked in a drying oven at 200°C for 6 h. The as-produced powders were then calcined in air at each designated temperature ranging from 600°C to 1200°C with the incremental temperature of 50°C for 5h in order to synthesize the $La_x$-5582 at each different temperature.

The calcined cakes of perovskite catalysts were ground with mortars to be dispersed better in aqueous solutions. The mixtures of desired catalyst inks were prepared by mixing physically 16 mg of catalyst powders with 0.2 mL of 5 wt% Nafion (Aldrich) solution and 0.8 mL of ethanol solution (≥99.5% purity), followed by ultrasonicating the mixture for 3 h in order to form homogeneous catalysts inks.

The mixtures of catalyst inks were prepared by physically mixing 16 mg of catalyst powders and 4 mg of KB (commercial Ketjenblack EC-600JD) with 0.2 mL of 5wt% Nafion (Aldrich) solution and 0.8 mL of ethanol solution (≥99.5% purity), followed by ultrasonicating the mixture for 3 h in order to form homogeneous catalysts inks. 5 μL of the catalysts ink was carefully dropped onto a polished glassy carbon (GC) electrode of 4 mm diameter (RRDE Pt Ring/GC Disk Electrode, cat. NO. 011162, ALS Co., Ltd.). Glassy carbon electrodes were polished with 0.05 μm polishing alumina to maintain a good condition of working electrode (PK-3 Electrode Polishing kit, ALS Co., Ltd.). Catalyst-coated GC electrodes were then dried under vacuum at room temperature for 3 h. In this study, the loading amount of all catalyst is 0.639 $mg_{ox}$ /$cm^2$, except for Pt/C 20% as a reference catalyst ink. All the composite materials are composed of catalyst materials ($La_x$-5582, and $IrO_2$) 80wt%/KB600 20wt%, so material names are simply mentioned in this study as $La_{0.1}$-1μm, $La_{0.7}$-100nm, $La_{0.7}$-50nm and $IrO_2$. The Pt/C 20% catalyst ink was made by dispersing Vulcan XC-72 catalysts (Premetek Co.) in a water-ethanol solution, of which 0.157 $mg_{Pt}$ /$cm^2$ was applied to electrodes. (Note this is an optimized procedure of the one reported in ref. 29). For precious metal-based oxide catalysts, $IrO_2$ (~5μm, Iridium(IV) oxide, Sigma-Aldrich 99.9%) was used as a reference material.

 

**Catalyst evaluation**

Rotating ring-disk electrode (RRDE) experiments were performed for 80wt% $La_x$-5582 on 0wt% Ketjenblack composites (BSCF5582) and 20wt% Pt on 80wt% Vulcan XC-72 composites (Pt/C 20%). All half-cell experiments for ORR using a rotating ring-disk electrode (RRDE) (ALS Co., Ltd.) were carried out under the same conditions with a 4 mm diameter working electrode where Pt wire and Hg/HgO were used as a counter and reference electrodes, respectively. 0.10 M KOH was used as an electrolyte; pure oxygen gas (99.9%) was purged for 30 min before each RDE experiment to make the electrolyte saturated with oxygen. Electrochemical characterization of as-prepared catalysts were conducted using bi-potentiostat (Iviumstat) with a scan rate of 10 mV/s at 1600 rpm with a potential range from 0.15 to -0.7 V vs. Hg/HgO under the saturated oxygen gas, and sufficient ring potential of 0.4 V was biased to oxidize immediately during ORR. Half-cell experiments for ORR using RRDE were carried out under the saturated argon gas for background measurements separately. Potential/V vs. RHE was obtained by adding 0.92 V to Potential/V vs. Hg/HgO. The collection efficiency (N) was determined under Ar atmosphere using 10 mM $K_3[Fe(CN)_6]$, which is around 0.41. This value is very close to its theoretical value, 0.42. Hydrogen peroxide yields and the number of electrons transferred (n) were calculated using the equations as below

$$HO_2(\%) = 200\,\frac{\frac{I_r}{N}}{I_d + \frac{I_r}{N}}$$

$$n = 4\,\frac{I_d}{I_d + \frac{I_r}{N}}$$

where the experimentally determined collection efficiency (N) was 0.41.

Rotating disk electrode (RDE) experiments for OER were performed for 80wt% $La_x$-5582 on 20wt% Ketjenblack composites (BSCF5582) and 80wt% $IrO_2$ on 20% Ketjenblack composites ($IrO_2$). All half-cell experiment for OER using a rotating disk electrode (RDE) (ALS Co., Ltd.) was carried out under the same conditions with a 4 mm diameter working electrode where Pt wire and Hg/HgO were used as a counter and reference electrodes, respectively. 0.10 M KOH was used as an electrolyte; pure oxygen gas (99.9%) was purged for 30 min before each RDE experiment to make the electrolyte saturated with oxygen. Electrochemical characterization of as-prepared catalysts was conducted using a bi-potentiostat (Iviumstat) with a scan rate of 10 mV/s at 1600 rpm with the potential range from 0.35 to 0.9 V vs. Hg/HgO.

Rotating disk electrode (RDE) experiments were executed for 80wt% $La_{0.7}$-50nm on 20wt% Ketjenblack composites to measure the lifetime of ORR and OER catalyst as chronoamperometric analysis. All half-cell experiments for ORR and OER using a rotating disk electrode (RDE) (ALS Co., Ltd.) were carried out under the same conditions with a 4 mm diameter working electrode where Pt wire and Hg/HgO were used as a counter and reference electrodes, respectively. 0.10 M KOH was used as an electrolyte; pure oxygen gas (99.9%) was purged for 30 min before each RDE experiment to make the electrolyte saturated with oxygen. Chronoamperometric characterization of as-prepared catalysts was executed using bi-potentiostat (Iviumstat) at 1600rpm with a scan rate of 10 mV/s at the fixed potential of 0.7 V (vs. RHE) and 1.5 V (vs. RHE) for ORR and OER, respectively.

**Material Characterization**

The crystal structures of the materials were analyzed by X-ray diffractometer (XRD) (D/Max2000, Rigaku) using Cu-Ka radiation, a scan range of 10°–100°, a step size of 0.02°, and a counting time of 5 s. Lattice parameters were determined using a least-squares method. The material morphology and structure were analyzed using a SEM (S-4800, Hitachi) operating at 10 kV and TEM (JEOL JEM-2100F) operating at 200 kV. The particle size distributions for histogram were analyzed by counting 80~100 number of identical particles under SEM (FEI) micrographs operating at 10 kV. Fe and Co K-edge X-ray absorption spectra of the perovskite La-doped BSCF5582 and a 100x electrochemically-cycled sample, X-ray absorption near edge structure (XANES) and extended X-ray absorption fine structure (EXAFS), were collected on BL10C beam line at the Pohang light source (PLS-II) with top-up mode operation under a ring current of 300 mA at 3.0 GeV. The monochromatic X-ray beam could be obtained using liquid-nitrogen cooled Si (111) and Si(311) double crystal monochromator (Bruker ASC) with *in-situ* exchange under the vacuum from high intense X-ray photons of multipole wiggler source. The Si(111) crystal pair has been used for Fe (absorption edge energy, 7112ev), Co (7709eV) K-edge XAFS measurements. The X-ray absorption spectroscopic data were recorded for the uniformly dispersed powder samples with a proper thickness on the polyimide film, in transmission mode with $N_2$ gas-filled ionization chambers as photon detectors. Higher order harmonic contaminations were eliminated by detuning to reduce the incident X-ray intensity by ~40%. Energy calibration has been simultaneously carried out for each measurement with reference metal foils placed in front of the third ion chamber. The data reductions of the experimental spectra to normalized XANES and Fourier-transformed radial distribution function (RDF) were

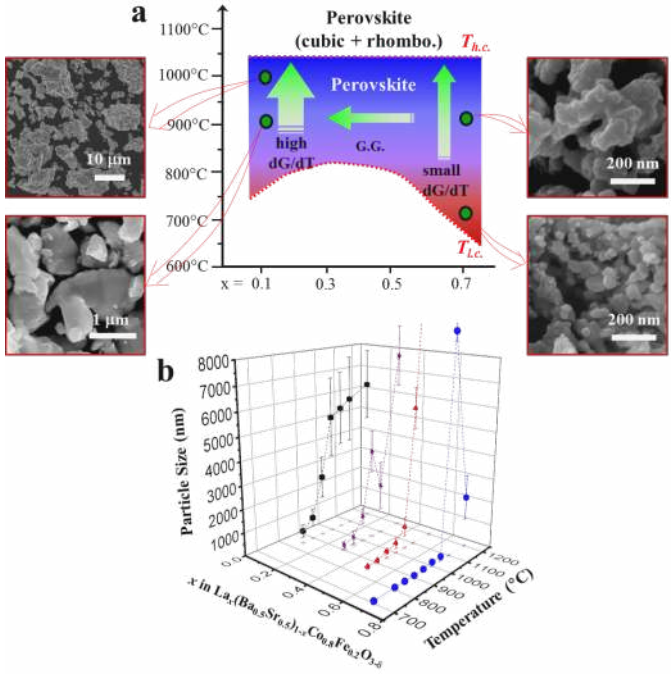


**Figure 1**. **(a)** Schematic diagrams phase against calcination temperature (°C) and La concentration (*x*) in $La_x(Ba_{0.5}Sr_{0.5})_{1-x}Co_{0.8}Fe_{0.2}O_{3-\delta}$ that describes the zone of stable cubic perovskite phases between high critical temperatures ($T_{h.c.}$) and low critical temperatures ($T_{l.c.}$). G.G. denotes grain growth. Arrows point in the direction of increasing particle size (see discussion in text). **(b)** The particle size as function of *x* and temperature.

performed through the standard XAFS procedure.

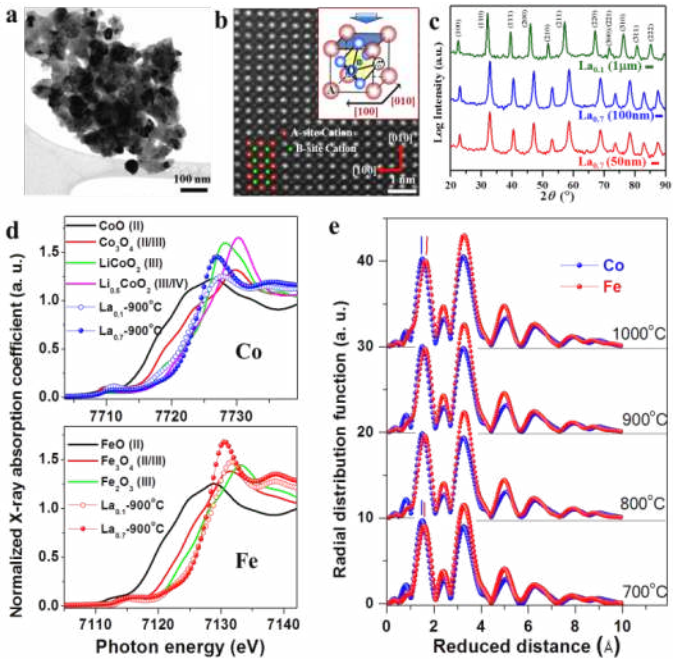


**Figure 2**. **a**) BFTEM image $La_{0.7}(Ba_{0.5}Sr_{0.5})_{0.3}Co_{0.8}Fe_{0.2}O_{3-\delta}$-50nm calcined at 700 °C for 5 h in air ($La_{0.7}$-50nm), **b**) HAADF STEM image showing the atomic arrangements of cubic perovskite structure in <100> direction and schematic of a perovskite unit cell, **c**) X-ray diffraction patterns for $La_{0.7}$-50nm, $La_{0.7}$-100nm and $La_{0.1}$-1μm, **d**) Normalized Co and Fe K-edge XANES spectra for $La_{0.7\_900°C}$ ($La_{0.7}$-100nm) (filled circles) and $La_{0.1\_900°C}$ ($La_{0.1}$-1μm) (open circles) and references, **e**) RDFs of Fourier-transformed $k^3$-weighted EXAFS spectra for $La_{0.7\_700°C}$ ($La_{0.7}$-50nm), $La_{0.7\_800°C}$($La_{0.7}$-70nm), $La_{0.7\_900°C}$ ($La_{0.7}$-100nm) and $La_{0.7\_1000°C}$.

## Results and discussion

On exploring the overall range of the calcination temperatures and La substitution, $x$, in $La_x(Ba_{0.5}Sr_{0.5})_{1-x}Co_{0.8}Fe_{0.2}O_{3-\delta}$, (La-BSCF), we discovered an interesting pattern of perovskite phase existence and particle growth (Figure S1). The phase diagram in Figure 1 shows that perovskite catalysts exist as pure cubic phases in the range between the higher critical temperature ($T_{h.c.}$) and the lower critical temperature ($T_{l.c.}$). Above the higher critical temperature ($T_{h.c.}$), the rhombohedral $LaCoO_3$ phase co-exists in the matrix of cubic perovskite phase, and above the lower critical temperature ($T_{l.c.}$), a cubic perovskite phase appears where the overall particle size decreases with the increasing substitution of La into La-BSCF (Figure S1-S4). As the calcination temperature decreases at La stoichiometry $x$ = 0.7, the calcined particle size decreased systematically from 100 nm at 900 °C to 50 nm at 700 °C in the HRTEM images of Figures S5 and S8. Generally, as $La_2O_3$ is doped into BSCF, the La cation is expected to occupy the lattice site of the A-site cations (Ba or Sr) and give rise to the oxidation of the B-site cation, preferentially in the Co-octahedron sublattice (Figure S1, Equation S1-2).[29] As the La concentration ($x$) increased from 0.1 to 0.7 at 900 °C, the Co K-edge XANES edge shifts towards the higher energy region while Fe K-edge XANES peak does not change, which demonstrates the preferential oxidation of Co sublattice octahedra with increasing La concentration (Figure 2d).

The interplay of defects with positive and negative effective charge is important to understand the structure and size of the oxide particles. The defect complexes formed above $T_{h.c.}$ in this study involve association between $La^{3+}$ cations (positive effective charge) and cobalt cations (effective negative charge), forming into a neutral complex defect (Figure S1 Equation 3).[29-31] With increasing concentration, these types of defects may order and form intergrown microdomains of a closely related perovskite phase, rhombohedral $LaCoO_3$ perovskite phase, which is analyzed in detail by X-ray diffraction, TEM EDS, TEM images,[29, 32, 33] and analysis of the extended X-ray absorption fine structure (EXAFS). Within the range

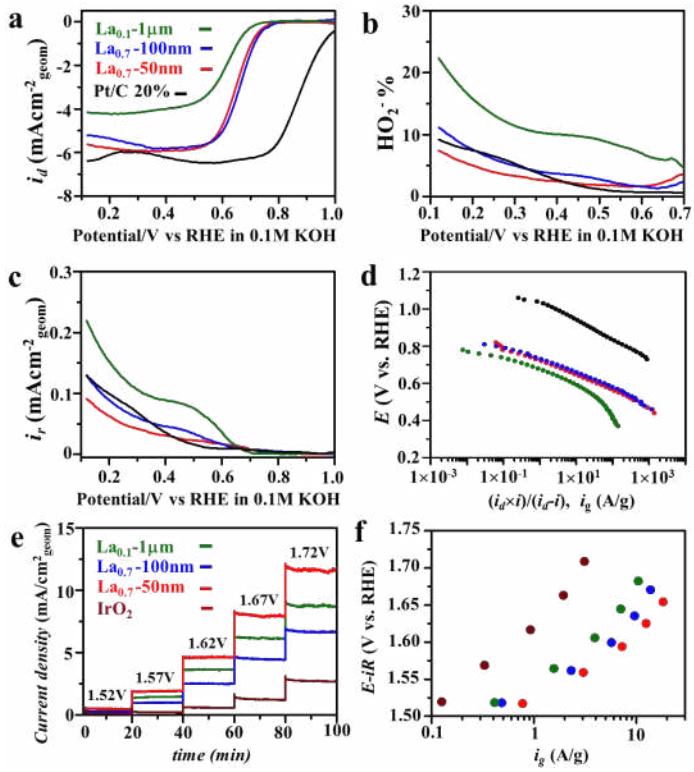


**Figure 3.** The properties of ORR and OER activities (capacitance-corrected) of $La_{0.1}(Ba_{0.5}Sr_{0.5})_{0.9}Co_{0.8}Fe_{0.2}O_{3-\delta}$ ($La_{0.1}$-1μm), $La_{0.7}(Ba_{0.5}Sr_{0.5})_{0.3}Co_{0.8}Fe_{0.2}O_{3-\delta}$-100nm ($La_{0.7}$-100nm) and La $_{0.7}(Ba_{0.5}Sr_{0.5})_{0.3}Co_{0.8}Fe_{0.2}O_{3-\delta}$-50nm ($La_{0.7}$-50nm) **(a)** disc and **(c)** ring currents (voltammograms) of the ORR and the determined **(b)** peroxide percentage ($HO_2^-$ %) and **(d)** Tafel plots of the gravimetric ORR activities as a function of potential in oxygen saturated 0.1 M KOH electrolyte at 10 $mVs^{-1}$ scan rate at 1600 rpm. **(e)** OER currents at select potentials and **(f)** Tafel plot of the gravimetric OER activities. The oxide electrode composites consist of 80 wt% oxide materials and 20 wt% KB, and Pt/C 20% consists of 20 wt% Pt and 80 wt% Vulcan XC-72(E-tek). Pt/C 20% (black line), $IrO_2$ (brown line), $La_{0.1}$-1μm (green line), $La_{0.7}$-100nm (blue line) and $La_{0.7}$-50nm (red line). The all oxide electrode composites contain 0.64 $mg_{ox}/cm^2_{disk}$, 0.16 $mg_{KB}/cm^2_{disk}$, 0.35 $mg_{Nafion}/cm^2_{disk}$, respectively, while Pt/C 20% electrode contains 0.16 $mg_{Pt}/cm^2_{disk}$, 0.64 $mg_{XC-72}/cm^2_{disk}$, 0.35 $mg_{Nafion}/cm^2_{disk}$, respectively. At least three independent measurements were executed in order to confirm the repeatability of the experimental results for each sample.

between $T_{h.c.}$ (~1050 °C) and $T_{l.c}$, a cubic perovskite phase exists uniformly as inferred from XRD (Figure S1). The local structure was

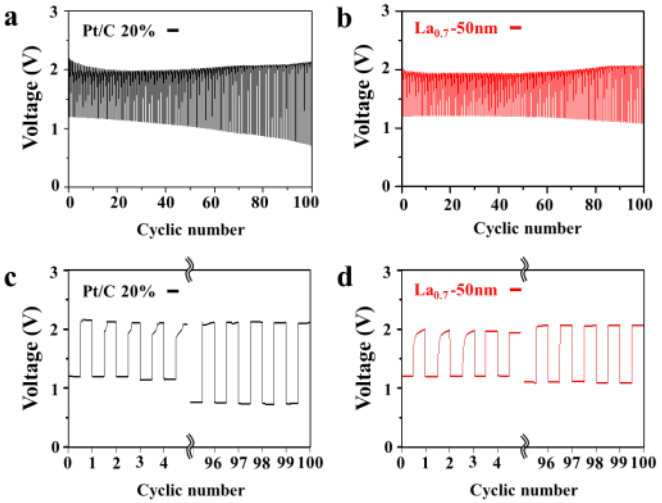


**Figure 4.** The repeated charge and discharge test as Zn-air full-cell under 10.5 $mAcm^{-2}$ in 6 M KOH with **(a)** Pt/C 20% and **(b)** La $_{0.7}(Ba_{0.5}Sr_{0.5})_{0.3}Co_{0.8}Fe_{0.2}O_{3-\delta}$-50nm ($La_{0.7}$-50nm) catalyst as short time cycle, where 1 cycle consists of the 300 s of discharging, followed by 300 s of charging, and comparison of the first and last 5 cycles for **(c)** Pt/C 20% and **(d)** $La_{0.7}$-50nm.

investigated by analysis and fitting of the Fourier-transform (FT) of the $k^3$-weighted EXAFS, where the peak position correlates with interatomic distances and the peak height correlates with the number of atoms sharing the same mean interatomic distance and the distribution of these distances. Therefore, the decrease of the EXAFS FT peak intensity at ~1.5 Å reduced distance indicated an increase of oxygen vacancies, and the EXAFS FT peak at ~3.5 Å suggested an effective decrease of long-range order for Co-O-Co and Co-O-A bond arrays (separate peaks not resolved in Fig. 2e and S6, but in simulation results of Table S1).[34] Moreover, the EXAFS FT separation between peak positions for the Co and Fe lattice increased with annealing temperature (Figure 2e and Table S1). This suggests that the sublattices are in the same phase at low temperature, while, at higher temperature, Co-O-Fe cation ordering (with short Co-O and long Fe-O) or separated formation of Co-rich phase could have started to develop in the perovskite structures (Figure S6, 7 and Table S1). In support of this, a secondary phase was detected by XRD above $T_{h.c.}$ (Figure S1).

The conditions for the formation of the cubic perovskite can be understood in terms of the activation energy ($Q$) obtained from the Arrhenius plot of the grain size (Figure S8). With increasing La concentration ($x$), $Q$ increased from 1.64 eV/atom at $x$=0.1 to 2.60 eV/atom-K at $x$=0.3 as an apex, from which $Q$ decreased to 0.34 eV/atom-K at $x$=0.7 (Figure S8 and Eq. S4). Thus, a higher $Q$ results in a wider range of calcination temperatures that produce a stable perovskite cubic phase. When $Q$ is reduced, both the particle size and the synthesis temperature decrease coincidentally.[35, 36] Considering that $Q$ is likely dependent not only on the concentration of oxygen vacancies but also on the crystal structure, we suggest that the diffusion paths required for ions to migrate during the calcination process are blocked with increasing La concentrations, abating particle growth rate.

Using the newly developed phase diagram (Figure 1), we selected several cubic perovskites of the La-BSCF family with promising properties for oxygen electrocatalysis. For clarity of presentation, they will be denoted by their La concentration and particle size. $La_{0.7}$-50nm was prepared by calcining at 700 °C for 5 h in air, and $La_{0.7}$-100nm and $La_{0.1}$-1μm were prepared at 900 °C in air, resulting in BET surface areas of 21.3 $m^2g^{-1}$, 4.2 $m^2g^{-1}$ and 1.2 $m^2g^{-1}$, respectively (Table S2). Figures 3(a-d) show the capacitance-corrected ORR activities of $La_{0.1}$-1μm, $La_{0.7}$-100nm and $La_{0.7}$-50nm mixed with 20 wt% Ketjenblack carbon (KB) using rotating ring-disk electrodes (RRDEs), in comparison with the reference Pt/C 20% that consists of 20 wt% Pt and 80 wt% Vulcan XC-72 (E-tek) (Figure S9). The linear sweep voltammograms of Figure 3(a) show that the onset potentials for ORR of $La_{0.1}$-1μm, $La_{0.7}$-100nm and $La_{0.7}$-50nm are 0.70, 0.72 and 0.72 V vs RHE, respectively, while Pt/C 20% is at 1.01 V vs RHE. Comparing with the limiting currents of Pt/C 20% with -6.1 $mAcm^{-2}$, the values decreased significantly from -4.2 $mAcm^{-2}$ of $La_{0.1}$-1μm to -5.9 $mAcm^{-2}$ of $La_{0.7}$-50nm, as particle size approached the nano scale, indicating optimal coverage and mass transport of the nanoparticles. The ORR overpotentials at 2 A/g are 0.70 V, 0.71 V, 0.66 V and 1.01 V for $La_{0.7}$-50nm, $La_{0.7}$-100nm, $La_{0.1}$-0.1μm and Pt/C, respectively (Fig. 3d). The gravimetric ORR activities were the highest reported among crystalline perovskite oxides (Table S4). Additionally, Figure 3(b) showed that the peroxide yield ($HO_2^-$ %) at kinetic region is suppressed on a greater scale from 15 % for $La_{0.1}$-1μm, 7 % of $La_{0.7}$-100nm to 5 % for $La_{0.7}$-50nm. This demonstrated that $La_{0.7}$-50nm is dominated by reduction of oxygen to water, which is quite comparable to Pt/C 20% (Figures S10- 12). This suggests that successful control of particle size into nanoscale can significantly enhance the gravimetric ORR activity and decrease the peroxide yield of BSCF-based perovskite catalysts.

The gravimetric OER activity is likewise enhanced when the particle size approached the nanoscale (Figure S13). The OER overpotentials at 2 A/g are 1.54 V, 1.56 V, 1.58 V and 1.67 V for $La_{0.7}$-50nm, $La_{0.7}$-100nm, $La_{0.1}$-0.1μm and $IrO_2$, respectively. Again, these gravimetric activities are among the highest reported for crystalline perovskite oxides (Table S4). In addition, Figures 3(e) and 3(f) show that the geometric and gravimetric OER activities of $La_{0.7}$-50nm were nearly five times higher and 20 time higher, respectively, as compared to commercial $IrO_2$, despite having a specific activity slightly lower than $IrO_2$ (Figure S13). This suggests that the significant enhancement of the gravimetric OER activity of La0.7-50nm is attributable to an increased number of activity sites through increased surface area, not from optimization of surface chemistry of the BSCF perovskite catalysts. The specific activity of these catalysts decreased when approaching nanoparticles (Figure S13), which is not understood. In summary, the successful synthesis of nanoscale perovskite catalysts contributed on a large scale to the simultaneous enhancement of both gravimetric ORR and OER activity for BSCF-based perovskite electrocatalysts in half-cell tests, particularly without any supportive reinforcement such as N-doped particle, CNT and graphite source. This achievement is of a great significance from the aspect of real application, for instance rechargeable Zn-air batteries are more robust against the structural degradation that is related with carbon decomposition.[17, 37-40]

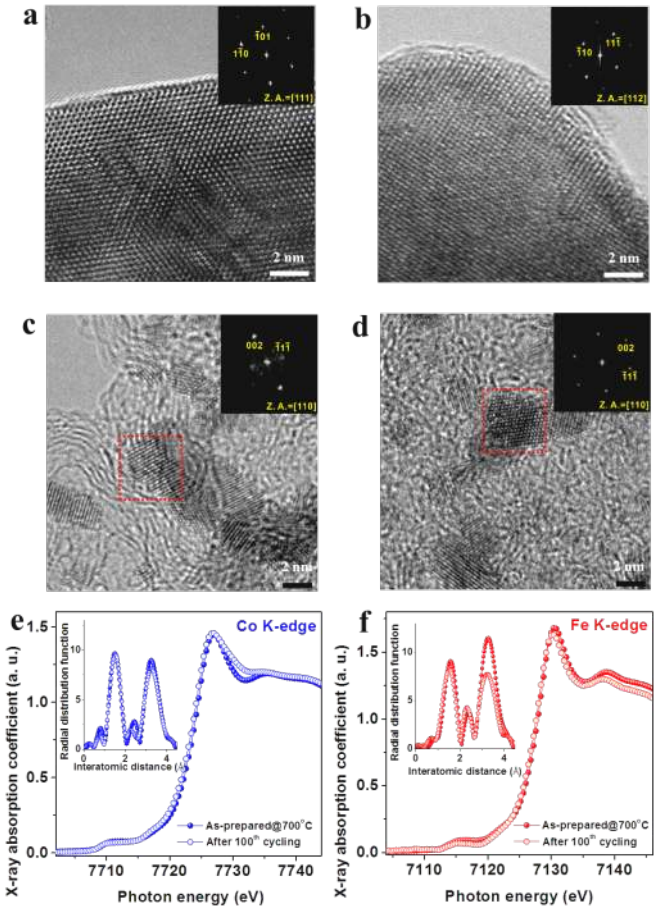


**Figure 5.** HRTEM images on the surfaces of $La_{0.7}(Ba_{0.5}Sr_{0.5})_{0.3}Co_{0.8}Fe_{0.2}O_{3-\delta}$-50nm particles **a**) before and **b**) after 100$^{th}$ cycle of the short time full-cell test, and Pt/C 20% particles **c**) before and **d**) after 100$^{th}$ cycle of the short time full-cell test. **e**) Co and **f**) Fe K-edge XAFS spectra of electrochemically 100$^{th}$ cycled sample for $La_{0.7}(Ba_{0.5}Sr_{0.5})_{0.3}Co_{0.8}Fe_{0.2}O_{3-\delta}$-50nm particles.

The availability of this catalyst for practical application was addressed by a zinc-air full-cell test, as shown in Figure 4, where the experiment was performed under 10.5 mAcm$^{-2}$ (2 A/$g_{ox}$ or 10 A/$g_{Pt}$) in 6 M KOH, making use of ambient air on the cathode side (Figure S16). We performed up to 100 cycles as either short or long duration cycling. For short duration cycling, one cycle consists of 10 min of discharging, followed by 10 min of charging (Figure 4), while for long duration cycling, one cycle consists of 60 min of discharging, followed by 60 min of charging (Figure S17). For Pt/C 20%, the overpotential difference between charge and discharge ($\Delta\eta$) increased from 0.80 V during the 1$^{st}$ cycle ($\Delta\eta_1$) to 1.50 V during the 100$^{th}$ cycle ($\Delta\eta_2$) ($\Delta=\Delta\eta_2-\Delta\eta_1=0.7$ V), while the potential difference for $La_{0.7}$-50nm only varied between 0.75 V and 1.0 V ($\Delta=\Delta\eta_2-\Delta\eta_1=0.25$ V), indicating superior activity and stability of the latter (Figure 4a,b). While we caution that full cell tests are difficult to compare, the overpotential difference and its minor increase with cycling (i.e. high stability) is as good as or better than other Zn-air battery chemistries in literature (Table S5).

Excellent stability of $La_{0.7}$-50nm is also supported by HRTEM analysis and XAFS. HRTEM before and after the 100$^{th}$ cycle of the short time full-cell test clearly reveals the absence of structural degradation or transformation such as surface amorphization, and neither was there any micro-structural change after and before 100$^{th}$ cycle in the short time full-cell test of Pt/C 20% as shown in Figure 5 (c,d) and Figure S18. XAFS at both the Co and Fe K-edge of $La_{0.7}$-50nm in Figure 5 (e) and (f) clearly shows a reduction of the edge position by 0.4 eV after 100 cycles relative to the pristine sample, as was observed previously for BSCF.[41] In contrast to BSCF, the absence of new peaks in the RDF indicates that the perovskite structure is retained during cycling (Table S3).[41] We note that the FT peaks associated with Fe-O-A and Fe-O-B decrease, which would indicate a reduction in order of the Fe sublattice, being subject of ongoing research. On the other hand, the gradual increase of $\Delta\eta$ during full-cell testing did not necessarily come from the degradation or phase change of catalyst particle itself, but could be from that of the carbon support. However, a more detailed investigation is required to fully explain this supposition.

The outstanding gravimetric activity of $La_{0.7}$-50nm in both OER/ORR half-cell and zinc-air full-cell tests as a bi-functional catalyst is attributable to the favorable electronic structure of B-site cations in BSCF-based perovskite catalysts, as well as to the increased surface area of the nano-sized perovskite catalyst. The successful synthesis of the nano-sized La-doped BSCF-based perovskite oxides in this study was contrived on the base of a deep understanding of the particle growth mechanism considering the perovskite defect chemistry. This approach resulted in the synthesis of 50 nm sized La-doped BSCF particles with a cubic perovskite structure. These particles represented outstanding ORR/OER performances in both half-cell and Zn-air full cell tests when compared with Pt/C 20%. This impressive performance of the $La_{0.7}$-50nm perovskite catalyst harbingers the conceivable application of BSCF-based bifunctional electrocatalysts in metal-air battery systems, which will result in rechargeable metal-air battery systems with high energy and power density. Our synthesis approach opens the gate for the development of further bi-functional nano-sized perovskite catalysts with high performance and stability. Such catalysts are urgently needed for the aggressive advancement of the renewable energy industry, particularly for rechargeable air batteries.

## Acknowledgements

This research was supported by the next-generation battery R&D program of MOTIE/KEIT, Korea (10042575), and was also partially funded by the Cooperative Agreement between the Masdar Institute of Science and Technology (Masdar Institute), Abu Dhabi, UAE and the Massachusetts Institute of Technology (MIT), Cambridge, MA, USA - Reference 02/MI/MIT/CP/11/07633/GEN/G/00, and also the Skoltech-MIT Center for Electrochemical Energy Storage, USA.

## Authors Contributions

J.I.J. and M.R. contributed equally as co-first authors.

## References

1. M. Armand and J. M. Tarascon, *Nature*, 2008, **451**, 652-657.
2. P. G. Bruce, S. A. Freunberger, L. J. Hardwick and J.-M. Tarascon, *Nat Mater*, 2012, **11**, 19-29.
3. R. Black, B. Adams and L. F. Nazar, *Advanced Energy Materials*, 2012, **2**, 801-815.
4. J.-S. Lee, S. Tai Kim, R. Cao, N.-S. Choi, M. Liu, K. T. Lee and J. Cho, *Advanced Energy Materials*, 2011, **1**, 34-50.
5. P. Pei, K. Wang and Z. Ma, *Applied Energy*, 2014, **128**, 315-324.

 

6. W. T. Hong, M. Risch, K. A. Stoerzinger, A. Grimaud, J. Suntivich and Y. Shao-Horn, *Energy & Environmental Science*, 2015, **8**, 1404-1427.
7. Y. Li and H. Dai, *Chemical Society Reviews*, 2014, **43**, 5257-5275.
8. R. Cao, J.-S. Lee, M. Liu and J. Cho, *Advanced Energy Materials*, 2012, **2**, 816-829.
9. F. Cheng and J. Chen, *Chemical Society Reviews*, 2012, **41**, 2172-2192.
10. S. Trasatti, *Electrochimica Acta*, 1991, **36**, 225-241.
11. S. Muller, K. Striebel and O. Haas, *Electrochimica Acta*, 1994, **39**, 1661-1668.
12. S. Muller, F. Holzer, H. Arai and O. Haas, *Journal of New Materials for Electrochemical Systems*, 1999, **2**, 227-232.
13. Y. Choi, M. C. Lin and M. Liu, *Angewandte Chemie International Edition*, 2007, **46**, 7214-7219.
14. M. Bursell, M. Pirjamali and Y. Kiros, *Electrochimica Acta*, 2002, **47**, 1651-1660.
15. C. K. Lee, K. A. Striebel, F. R. McLarnon and E. J. Cairns, *Journal of the Electrochemical Society*, 1997, **144**, 3801-3806.
16. S. Malkhandi, B. Yang, A. K. Manohar, A. Manivannan, G. K. S. Prakash and S. R. Narayanan, *The Journal of Physical Chemistry Letters*, 2012, **3**, 967-972.
17. Z. Chen, A. Yu, D. Higgins, H. Li, H. Wang and Z. Chen, *Nano Letters*, 2012, **12**, 1946-1952.
18. J. Suntivich, K. J. May, H. A. Gasteiger, J. B. Goodenough and Y. Shao-Horn, *Science*, 2011, **334**, 1383-1385.
19. M. Risch, K. A. Stoerzinger, S. Maruyama, W. T. Hong, I. Takeuchi and Y. Shao-Horn, *J Am Chem Soc*, 2014, **136**, 5229-5232.
20. J. Suntivich, H. A. Gasteiger, N. Yabuuchi, H. Nakanishi, J. B. Goodenough and Y. Shao-Horn, *Nature Chemistry*, 2011, **3**, 546-550.
21. Y. Matsumoto, H. Yoneyama and H. Tamura, *Journal of Electroanalytical Chemistry and Interfacial Electrochemistry*, 1977, **83**, 237-243.
22. Y. Matsumoto, H. Yoneyama and H. Tamura, *Journal of Electroanalytical Chemistry and Interfacial Electrochemistry*, 1977, **79**, 319-326.
23. J.-I. Jung and D. D. Edwards, *Journal of Solid State Chemistry*, 2011, **184**, 2238-2243.
24. S. McIntosh, J. F. Vente, W. G. Haije, D. H. A. Blank and H. J. M. Bouwmeester, *Chemistry of Materials*, 2006, **18**, 2187-2193.
25. J.-I. Jung and D. Edwards, *J Mater Sci*, 2011, **46**, 7415-7422.
26. D. N. Mueller, R. A. De Souza, T. E. Weirich, D. Roehrens, J. Mayer and M. Martin, *Physical Chemistry Chemical Physics*, 2010, **12**, 10320-10328.
27. J.-I. Jung, H. Y. Jeong, M. G. Kim, G. Nam, J. Park and J. Cho, *Advanced Materials*, 2015, **27**, 266-271.
28. N. Ortiz-Vitoriano, I. Ruiz de Larramendi, I. Gil de Muro, J. I. Ruiz de Larramendi and T. Rojo, *Materials Research Bulletin*, 2010, **45**, 1513-1519.
29. J.-I. Jung, H. Y. Jeong, J.-S. Lee, M. G. Kim and J. Cho, *Angewandte Chemie International Edition*, 2014, **53**, 4582-4586.
30. A. N. Petrov, O. F. Kononchuk, A. V. Andreev, V. A. Cherepanov and P. Kofstad, *Solid State Ionics*, 1995, **80**, 189-199.
31. G. King and P. M. Woodward, *Journal of Materials Chemistry*, 2010, **20**, 5785-5796.
32. L. Farber and P. Davies, *Journal of the American Ceramic Society*, 2003, **86**, 1861-1866.
33. C. A. Randall, A. S. Bhalla, T. R. Shrout and L. E. Cross, *Journal of Materials Research*, 1990, **5**, 829-834.
34. D. C. Koningsberger, B. L. Mojet, G. E. van Dorssen and D. E. Ramaker, *Topics in Catalysis*, 2000, **10**, 143-155.
35. S. Shukla, S. Seal, R. Vij and S. Bandyopadhyay, *Nano Letters*, 2003, **3**, 397-401.
36. E. R. Leite, M. A. L. Nobre, M. Cerqueira, E. Longo and J. A. Varela, *Journal of the American Ceramic Society*, 1997, **80**, 2649-2657.
37. T. Nagai, S.-i. Yamazaki, M. Asahi, Z. Siroma, N. Fujiwara and T. Ioroi, *Journal of Power Sources*, 2015, **293**, 760-766.
38. D. U. Lee, M. G. Park, H. W. Park, M. H. Seo, V. Ismayilov, R. Ahmed and Z. Chen, *Electrochemistry Communications*, DOI: http://dx.doi.org/10.1016/j.elecom.2015.08.001.
39. H. W. Park, D. U. Lee, P. Zamani, M. H. Seo, L. F. Nazar and Z. Chen, *Nano Energy*, 2014, **10**, 192-200.
40. Y. Xu, A. Tsou, Y. Fu, J. Wang, J.-H. Tian and R. Yang, *Electrochimica Acta*, 2015, **174**, 551-556.
41. M. Risch, A. Grimaud, K. J. May, K. A. Stoerzinger, T. J. Chen, A. N. Mansour and Y. Shao-Horn, *The Journal of Physical Chemistry C*, 2013, **117**, 8628-8635.


## TOC figure

The successful synthesis of a bifunctional perovskite electrocatalyst of ~50 nm size towards the development of energy storage systems with high power density.

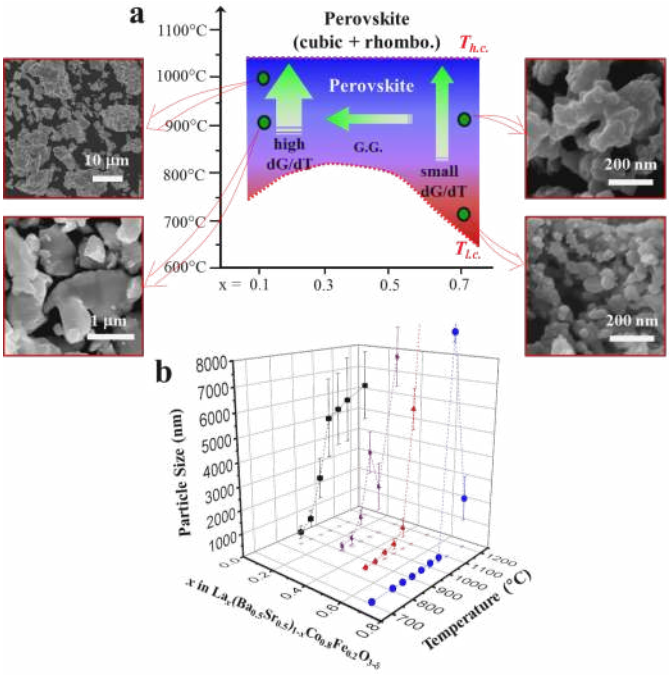


**(6.75 cm X 4 cm)**